



Flashing flow in the rotating curved channels with variable cross-section of a two-phase flow turbine

Hongyang Li, Zhibin Yu^{*}

James Watt School of Engineering, University of Glasgow, Glasgow G12 8QQ, UK

ARTICLE INFO

Keywords:

Flashing flow
Two-phase turbine
Vapour ring
Secondary flow

ABSTRACT

The rotating flash flow has rarely been studied, although its characteristics affect significantly the performance of the two-phase flow turbine. In this paper, through analyzing the flashing flow obtained by CFD methods, which is validated with the experimental data, the relationships of average flow parameters under various rotational speeds were studied theoretically and numerically using the flow equations established on the Frenet coordinate system. The ratio of the mass flow rate under various rotational speeds was formalized and found to be dependent on the rotational speed and thermophysical properties. The generation and development of vapour were revealed and correlated to the geometry of the channel. The secondary flow in the flashing rotating channel was discussed and found to rotate in opposite directions upstream/downstream of the throat. The flashing induced near the throat had the effect on flow homogenizing in the normal direction of the cross-section. The analysis could be further applied to the analogy of the secondary flow between the rotating single-phase flow and the rotating flashing flow.

1. Introduction

The stationary flashing flow can take place in various industrial equipment, such as pipelines in nuclear plants [1], fuel injectors [2,3], CO₂ ejectors [4], desalination chambers [5], safety valves [6,7], water and liquid nitrogen spray [8,9], converging-diverging nozzles [10,11], and so on. The rotating flashing flow appears in the utilization of LNG's cold exergy [12], supercritical compressed air energy storage system [13], geothermal turbines [14,15], and so on. However, there is little research on the flashing flow characteristics in the curve rotating channel.

The flashing flow in stationary channels has been studied theoretically, numerically, and experimentally so far. The nucleation theory [16–19] has proved to be essential for the closure and accuracy of the flow equations. The critical mass flow rate under the choking conditions was correlated with working conditions and thermophysical properties by Leung [20], Angielczyk et al. [21], and Leung and Grolmes [22]. Through studying the pressure profile along the flow direction, the pressure undershoot phenomenon was found and correlated by Jones [23], Alamgir and Lienhard [24], and Attou and Seynhaeve [25]. The pressure profile and the bubble evolution of the flashing flow in pipes and nozzles were revealed using pressure sensors and high-speed cameras. Abuaf et al. [26] presented pressure profiles in a series of converging-diverging nozzles

under various working conditions through experiments, which were extensively used in many numerical studies to validate mathematical models. Manera et al. [27] visualized the flow pattern under both stationary and transient conditions using wire-mesh sensors. Using high-speed cameras, Wang et al. [28] and Gärtner et al. [29] studied the flashing spray of R134a and liquid nitrogen, respectively. Due to the complexity and difficulty in studying the flashing process experimentally, many researchers developed numerical methods to simulate flow features and to design flow channels. Liao and Lucas [11] reviewed the application of CFD in studying flashing flow. As revealed in previous researches [30–37] about the flashing flow profile in stationary channels, there is a vapour ring generated at the throat of the channel, which develops along with the flow or disappears after a certain distance depending on the geometry. The vapour ring is a kind of annular flow regime caused by the heterogeneous nucleation of the bubble near the wall and the sudden change of the geometry. Rane and He [38] showed the vapour ring in the rotating channel designed by Date et al. [39], and Li et al. [15] revealed the vapour ring could exist in the square channel with the gradually changing geometry near the throat.

However, there is little research on the flashing flow in the rotating channel and the flow features have not been analyzed in detail. For a long time, there were several challenges in the study of the rotating

^{*} Corresponding author.

E-mail addresses: Hongyang.Li@glasgow.ac.uk (H. Li), Zhibin.Yu@glasgow.ac.uk (Z. Yu).

<https://doi.org/10.1016/j.icheatmasstransfer.2021.105434>

flashing flow. Firstly, it was hard to measure or predict the flow parameters of the liquid-vapour mixture in rotating channels. Secondly, it was hard to control the flashing process and there were few mathematical models for the rotating flashing flow. Thirdly, the pressure undershoot phenomenon affected the pressure distribution and the flow rate significantly. Although Date et al. [39] published the experimental performance of the two-phase reaction turbine and Rane and He [38] simulated the rotating flashing flow in this turbine, it can be found that in the flashing rotational channel, the variation of the mass flow rate under various rotational speeds has not been fully understood, the vapour ring has not been studied, and the secondary flow has not been revealed.

In the present paper, the rotating flashing flow in a two-phase flow turbine was investigated analytically for the first time. Firstly, the flashing flow field in a two-phase flow turbine was analyzed numerically based on the flashing models proposed by Rane and He [38] and compared with the experimental data published by Date et al. [39], and the vapour ring and liquid attachment effects were provided and analyzed. Secondly, the flow mechanism of the effects was demonstrated based on rotating flow formulas derived for the internal rotating flashing flow in the curved channel with varying cross-sections under various rotational speeds. This paper demonstrates the flow features of the rotating flashing flow and explains them by using an analytical method. To our best knowledge, this kind of study has not been reported in open literature so far.

In this paper, Section 2 describes the geometry model of the flashing rotating channel in the tested two-phase turbine, as well as simulation

methods and results. In Section 3, average flow parameters and the vapour ring are presented. The relationship of the flow parameters under various rotation speeds, the distribution of the vapour volume fraction and the secondary flow are explained in Section 4.

2. Model and validation

The flashing rotating channel was applied in the two-phase reaction turbine tested by Date et al. [39], as shown in Fig. 1(a). CFD methods are applied to simulate the flashing flow in the tested turbine and validated with the experimental data. Therefore, the detailed flow information of the rotating flashing flow can be obtained.

In the experimental research of Date et al. [39], the liquid flows into the test section through a tube that is mounted on the bottom of the turbine. Inside the turbine, as shown in Fig. 1(b), a mechanical seal is installed between the tube and the impeller entrance to prevent leakage through the gap. After entering the rotating impeller, the liquid flows along the channel of the impeller and vaporizes near the throat, as shown in Fig. 1(c) and (d). The two-phase mixture leaves the impeller at the outlet of the channel and enters the case of the turbine. Then, the two-phase mixture flows along a vacuum vessel, which is installed above the turbine. After leaving the vessel, the two-phase flow is condensed in the condenser.

Fig. 1(d) is the photograph of the machined impeller. There are two channels in the impeller. The subcooled liquid enters each channel at the inlet and flows along the channel. The shape of the cross-section is

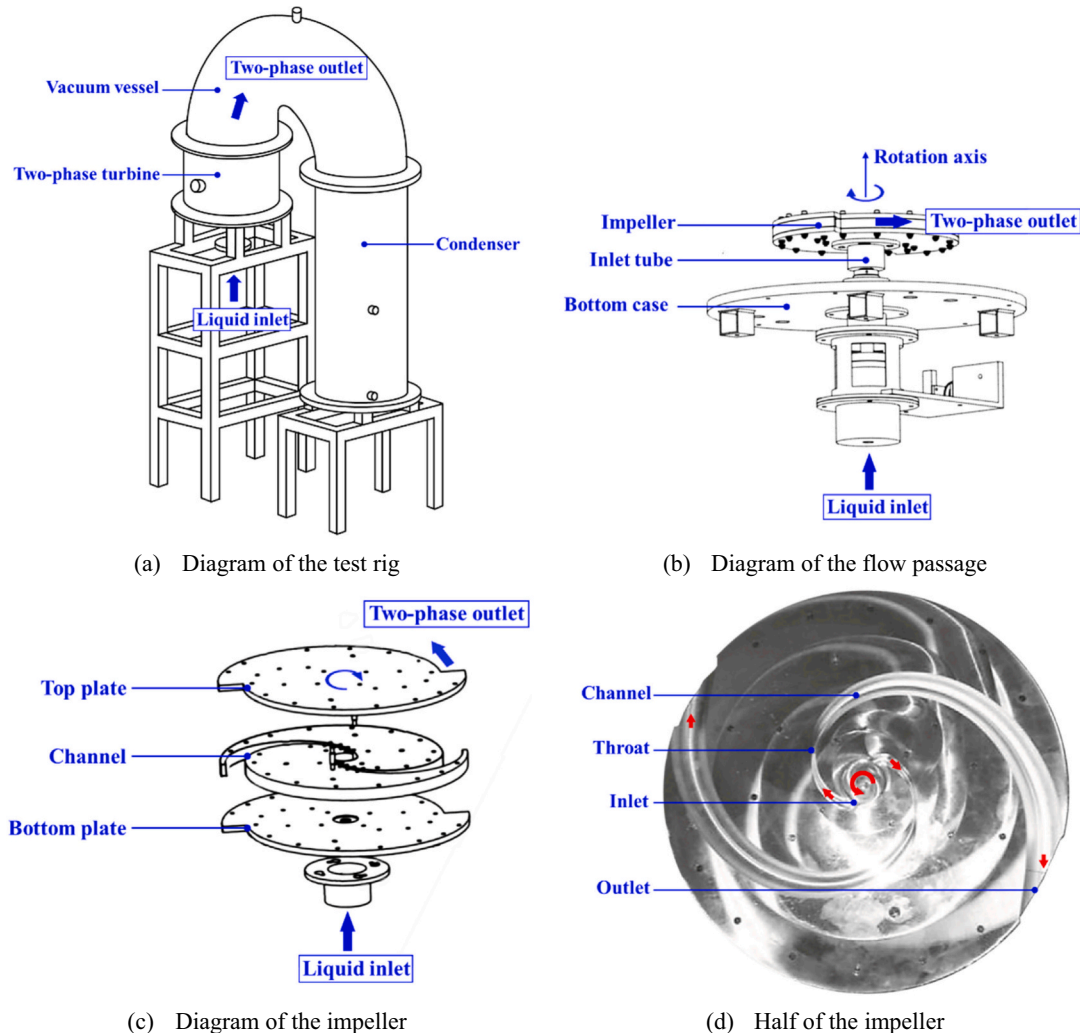


Fig. 1. Configuration of the two-phase turbine test rig and the channel of the impeller [39,40].

circular, and the radius of the cross-section decreases from the inlet to the throat. The liquid vaporizes near the throat. From the throat to the outlet of the channel, the radius of the cross-section increases, and the flashing flow further develops. The detailed geometry information and the experimental data of the turbine were published by Date et al. [39]. The distance between the center of the throat and the rotating center is 59 mm and the radius of the impeller is 150 mm. In the experiment, the inlet pressure, the inlet temperature, the flow rate, the outlet pressure and the output power are measured. The rotational speed in the experiment increases to 7306 rpm, while the design rotational speed for the impeller is 20,000 rpm.

The flashing flow in this impeller has been simulated using CFX software by Rane and He [14,38,41,42]. In the simulation, mathematical models are validated with the experimental data. The rotating flow passage includes a short section of the inlet tube, the channels and a part of the chamber between the case and the impeller. A quarter of the flow passage is simulated because there are two channels in the impeller and the geometry of the channel is symmetric about the mid-plane. Thus, the symmetric boundary is set at the mid-plane of the flow passage, and two periodic boundaries are set in the chamber, as shown in Fig. 2. The wall of the channel in the computational domain is divided into two parts for convenience: the wall facing the direction of the rotation is called the pressure side and the wall facing the opposite direction of the rotation is called the suction side. The pressure inlet and the pressure outlet are set at the inlet and the outlet of the domain, separately. The volume fraction and the temperature are also given at the inlet boundary. In both the simulation and the experiment, the inlet absolute pressure is 400 kPa, the inlet temperature is about 117 °C and the outlet pressure is 7.7 kPa.

In the simulation, the liquid water is set as the continuous phase and the vapour water is set as the dispersed phase. Shear Stress Transport turbulence model is used, and the heat transfer model is dependent on the fluids. The liquid temperature is solved through conservation equations and the vapour temperature is always equal to the local saturation temperature, which is determined by the local pressure of the fluid. Thermophysical properties of the liquid water and the liquid vapour are obtained using IAPWS-97. The Nusselt number for the heat transfer between the liquid and the vapour is derived using the thermal phase changing method, which is recommended for simulating the flashing flow in stationary nozzles by Liao and Lucas [43]. The initialization is highly related to the divergence of the simulation and Rane and He [38] proposed the initialization method of the pressure, volume fraction and temperature.

The validation of the simulation is illustrated in Fig. 3. The mass flow rate increases with the rotational speed. The predicted mass flow rate agrees with the experimental results, and the deviation between the CFD and the experiment decreases with the rotational speed, as shown in Fig. 3(a). The tested output power of the turbine increases with the rotational speed if the rotational speed is lower than 4623 rpm and keeps constant when the rotational speed increases from 4944 rpm to 5786

rpm. The output power can reflect the trends of the experimental results. The deviation between the CFD and the experiment reaches the minimum when the rotational speed is 4623 rpm, as shown in Fig. 3(b). The detailed flow field of the simulation results is analyzed detailed in the following sections.

3. Simulation results

The validated CFD model is then used to obtain the flashing flow field and analyze flow features in the channel of the turbine, including the average flow parameters and the vapour ring. The obtained results are presented and discussed in this section.

3.1. Average rotating flashing flow parameters

Average flow parameters are calculated on cross-sections that are normal to the center line of the channel, as shown in Fig. 4. The channel rotates about the w-axis which is in the Cartesian coordinate system based on the origin point. Thus, the distribution of flow parameters on cross-sections can reflect average flow characteristics along the channel.

The averaged pressure profiles on cross-sections are shown in Fig. 5 (a). The horizontal axis is the radius of the center line used to identify the location of the cross-section. Before the throat, the pressure increases along the direction of the center line and the magnitude of the pressure gradient increases with the rotational speed. Before the throat, the subcooled liquid is not vaporized significantly, and the rotating liquid flow may be similar to the flow in pumps. However, it does not mean that the pressure must increase before the throat. The pressure could decrease along the flow direction, and the subcooled liquid flow may be similar to the flow in liquid turbines before the throat. Whether the pressure should increase or decrease is determined by the rotational speed and the design angle of the center line, which can be used to derive the relative flow angle. A significant difference in the pressure distribution between the rotating flashing flow and the rotating single-phase flow is the large pressure gradient near the throat, where the pressure decreases significantly to a specific pressure (63–65 kPa) which is higher than the outlet pressure (7.7 kPa), but far less than the local vaporization pressure (181 kPa). The specific pressure is almost constant among various rotational speeds. The large pressure drop can be related to the pressure undershoot phenomenon of the flashing flow in convergent-divergent nozzles. After the throat, the pressure decreases gradually along the flow direction.

The averaged liquid relative velocity profiles are shown in Fig. 5(b). Before the throat, the velocity and the magnitude of the velocity gradient increase along the direction of the center line under a certain rotational speed. Near the throat, the velocity reaches the local peak, which increases with the rotational speed. After the throat, the velocity does not increase any more but keeps almost constant if the radius is between 59 and 65 mm. After the throat, the velocity continues to

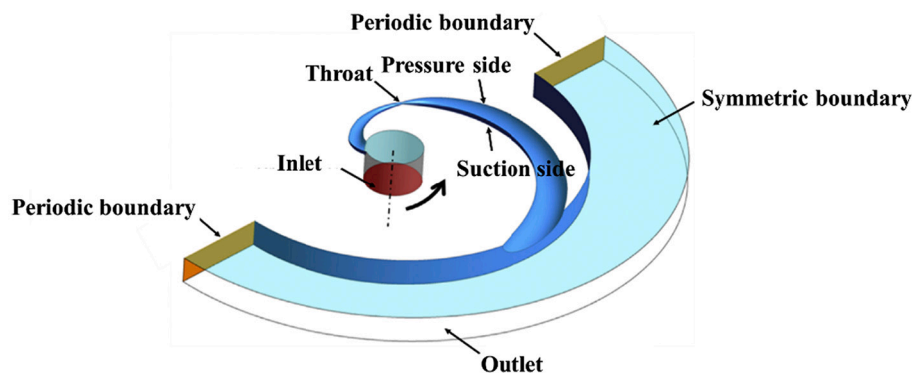


Fig. 2. Computational domain and boundary conditions [38].

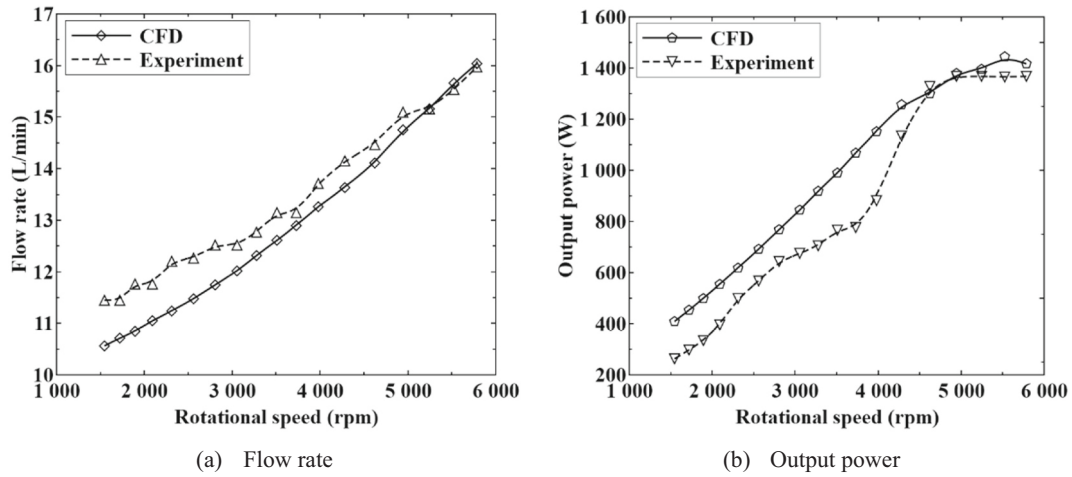


Fig. 3. Comparison of the flow rate and the output power between CFD and experiment.

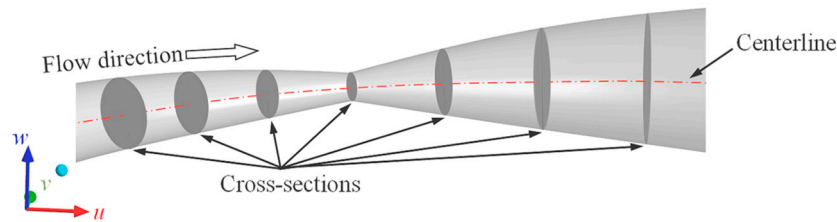


Fig. 4. Cross-sections in the channel for analysis.

increase gradually until the radius reaches 123 mm. But for the rotational speed higher than 3055 rpm, the velocity still increases near the outlet. It should be noted that under the constant inlet pressure and inlet temperature, the liquid relative velocity determines the mass flow rate. Thus, the ratio of the liquid relative velocity near the inlet is equal to the ratio of the mass flow rate. But after the throat, the liquid vaporizes significantly and the density of the mixture decreases significantly, so the ratio of the liquid relative velocity downstream the throat cannot determine the ratio of the mass flow rate any more.

The averaged liquid absolute velocity profiles are shown in Fig. 5(c). The variation of the absolute velocity is determined by the relative velocity, the relative flow angle and the circumferential velocity. Near the inlet, the liquid relative velocity is much lower than the circumferential velocity. Thus, the liquid absolute velocity is almost equal to the circumferential velocity near the inlet. However, the liquid absolute velocity near the throat decreases due to the variation of the liquid relative velocity and the relative flow angle.

The averaged vapour volume fraction profiles are shown in Fig. 5(d). Near the inlet, there is slight vaporization due to the change of the geometry since the vapour volume fraction is larger than zero when the radius is about 25 mm. The vapour generation becomes significant at the throat, but the gradient of the vapour volume fraction decreases along the direction of the center line after the throat. The deviation of the vapour volume fraction is low among various rotational speeds.

According to the mathematical models presented by Rane and He [38] and Li et al. [15], the driving force of the vaporization includes the superheat degree of the liquid and the slip ratio. The Nusselt number Nu determines the heat transfer rate between the liquid and the vapour and can be expressed as

$$Nu = \frac{12}{\pi} Ja + 2\sqrt{\frac{Pe}{\pi}} \quad (1)$$

The first term on the right of Eq. (1) represents the effect of the superheat degree of the liquid Nu_{Ja} on the flashing, while the second term

represents the effect of the slip ratio Nu_{Pe} . The average Nusselt numbers along the flow direction are illustrated in Fig. 6 under various rotational speeds. The Nusselt number decreases as the rotational speed increases. After the throat, the vaporization is triggered, and the Nusselt numbers jump to high values and increases along the flow direction. Nu_{Ja} is almost 2/3 of Nu and plays a dominant role in vaporization. The effect of Nu_{Pe} cannot be neglected because it accounts for 1/3 of Nu .

3.2. Vapour ring

The triggering stems from the wall of the throat and develops from the wall into the inner core of the flow as shown in Fig. 7. The left side is the pressure side, and the right side is suction side from Fig. 7(b) to (m). The liquid in the inner core results from the inertial effect, while the vapour generation near the wall is caused by the low local pressure. Thus, the vapour near the throat forms a ring because the cross-section of the channel is circular. The vapour ring is generated at the throat which is Plane 1 and develops along the center line as shown in Fig. 7(b) to (m). Before Plane 5, the size of the liquid core is almost constant and the liquid volume fraction decreases along with the flow in the liquid core, as shown in Fig. 7(a). After Plane 5, the vapour develops significantly into the liquid core and the liquid core is almost invisible in Plane 12. It can also be found that the inner shape of the vapour ring is not a perfect circle due to rotating and geometrical effects. As shown in Fig. 7(c) and (d), the thickness of the vapour ring is larger near the pressure side than that near the suction side, because the inner liquid core turns a lower angle than the angle of the center line under the inertial effect.

3.3. Backflow in the ring

There are low-speed regions near the pressure line and suction line after the throat as shown in Fig. 8(a). Fig. 8(b) to (m) show the liquid relative velocity projected on the centerline direction in cross-sections normal to the centerline direction. It can be found that the low-speed

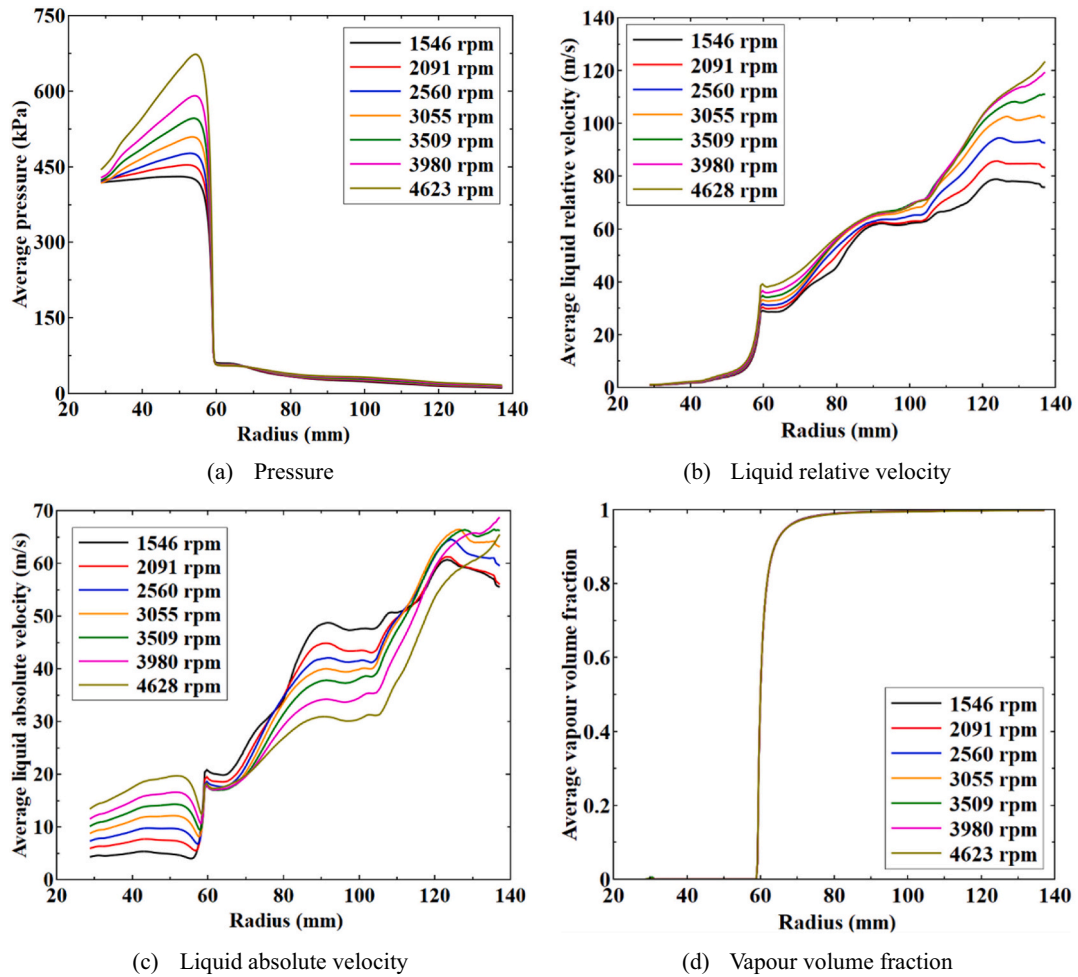


Fig. 5. Distribution of flow parameters along the direction of the center line under various rotational speeds.

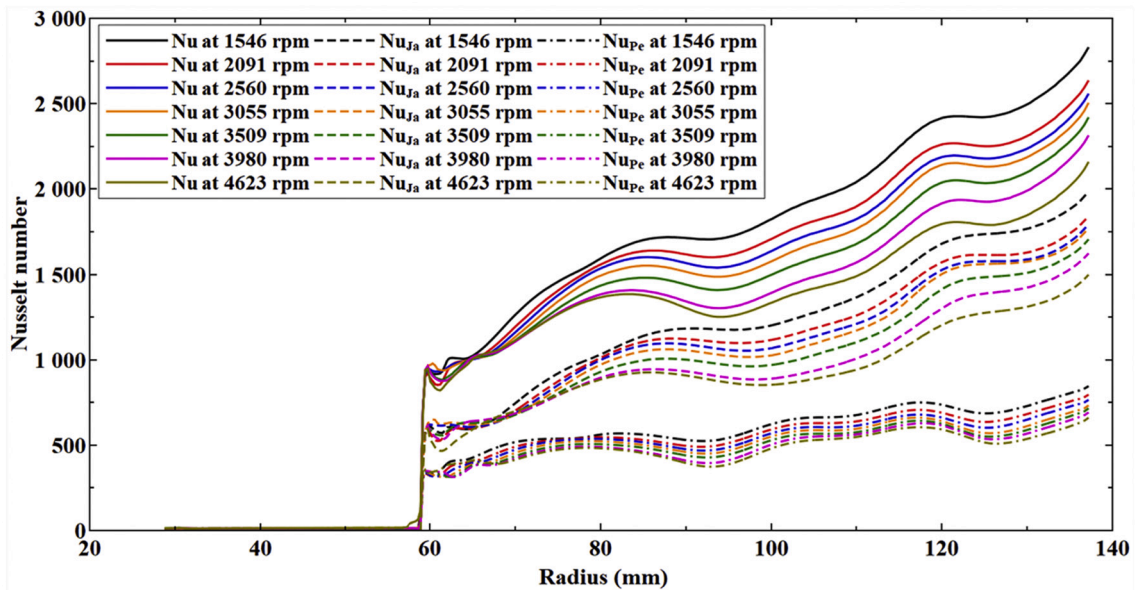


Fig. 6. Nusselt number under various rotational speeds.

region is ringlike inside the vapour ring, the thickness of the low-speed region is higher near the suction side than the pressure side, and the liquid velocity in the liquid core is almost constant. The size of the low-

speed region shrinks from the top and bottom of the cross-section to the suction line as shown in Fig. 8(e) to (h). However, the shrinking process is not uniform along the wall. The high-speed regions shrink along the

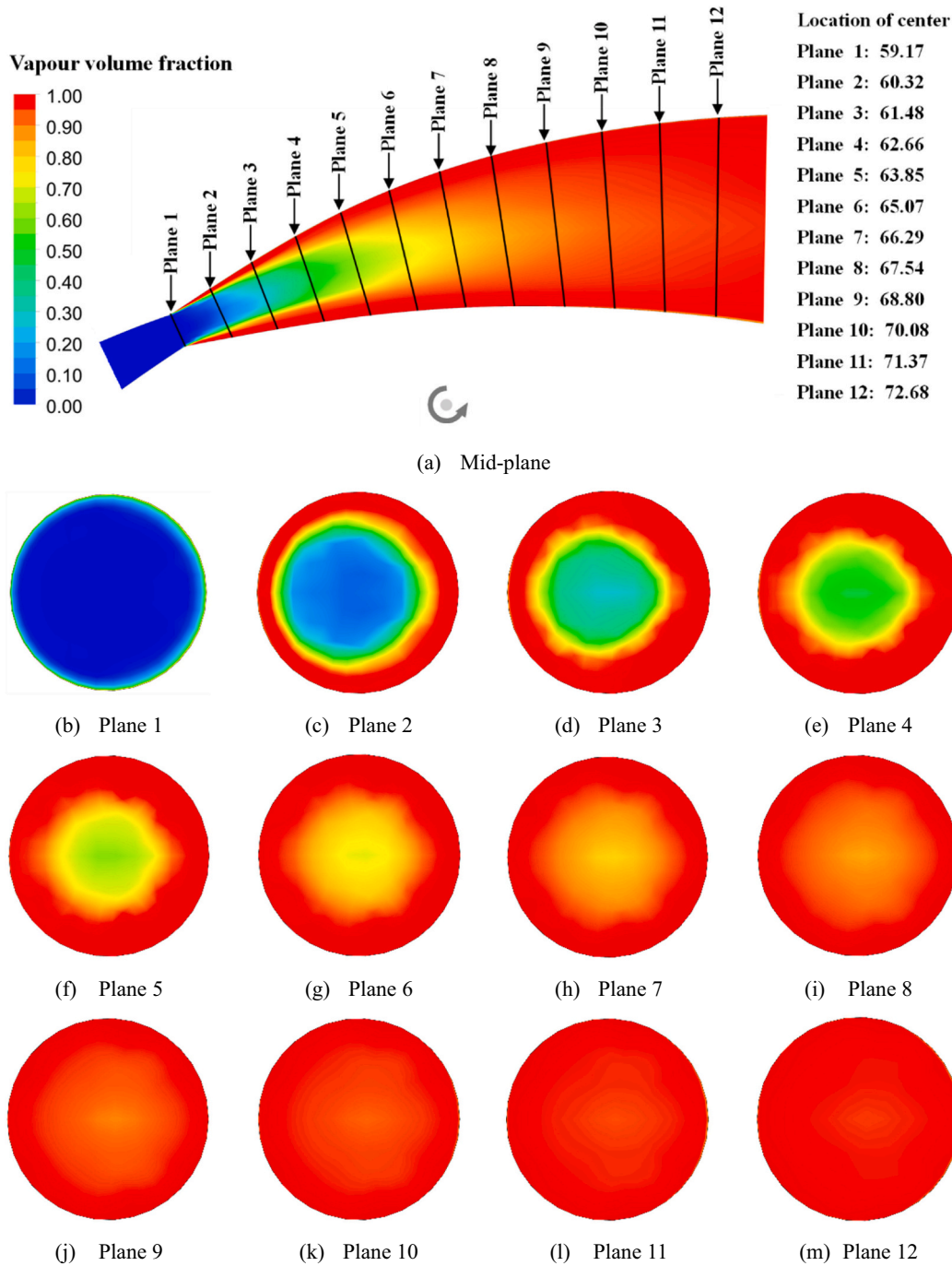


Fig. 7. Vapour volume fraction in cross-sections near the throat at 4623 rpm.

flow direction. It should be noted that the minimum liquid relative velocity is lower than zero in the low-speed region, as shown from Fig. 8(c) to (g), which indicates that the liquid in these regions flows backwards.

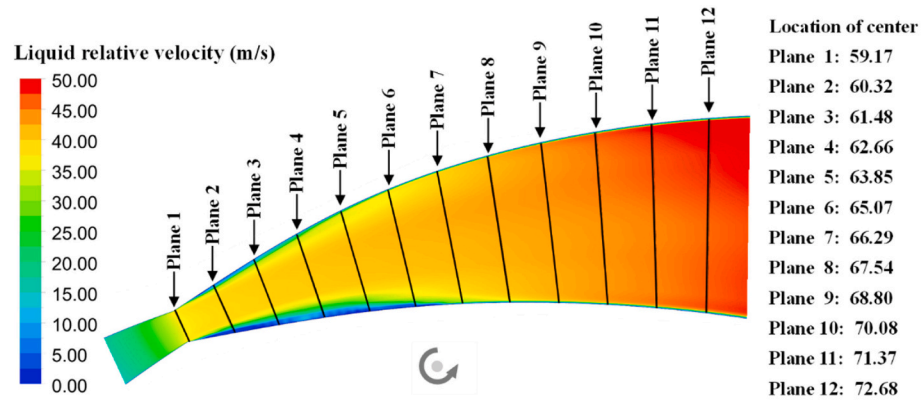
Fig. 9 show the vapour relative velocity near the throat. Due to the sudden change of the geometry at the throat and the inception of the vapour, the vapour relative velocity is high near the throat. There are also low-speed regions after the throat near the wall, as shown in Fig. 9 (a). The size of the low-speed region of the vapour is lower than that of the liquid as shown from Fig. 9(c) to (f). The vapour is generated significantly in the vapour ring and the liquid relative velocity is high in the liquid core, so there is a ring of high vapour speed region inside the vapour ring, as shown in Fig. 9(g). The high vapour speed region shrinks from Fig. 9(h) to (m) and causes high liquid speed regions shown from Fig. 8(g) to (h).

4. Further analysis of the results

The flashing flow features in the rotating channel can be further explained using two-phase flow equations. In this section, the flow equations are built, ratios of average flow parameters under various rotational speeds are analyzed, and the secondary flow in the channel is discussed.

4.1. One-dimensional governing equations for rotating flashing flow

In this section, a one-dimensional method was employed to identify the flashing flow mechanism of vapour ring. The rotating flashing flow can be analyzed in the Frenet coordinate system as shown in Fig. 10. The x-axis is the centerline of the channel and the y-axis is normal to the



(a) The magnitude of liquid relative velocity on mid-plane

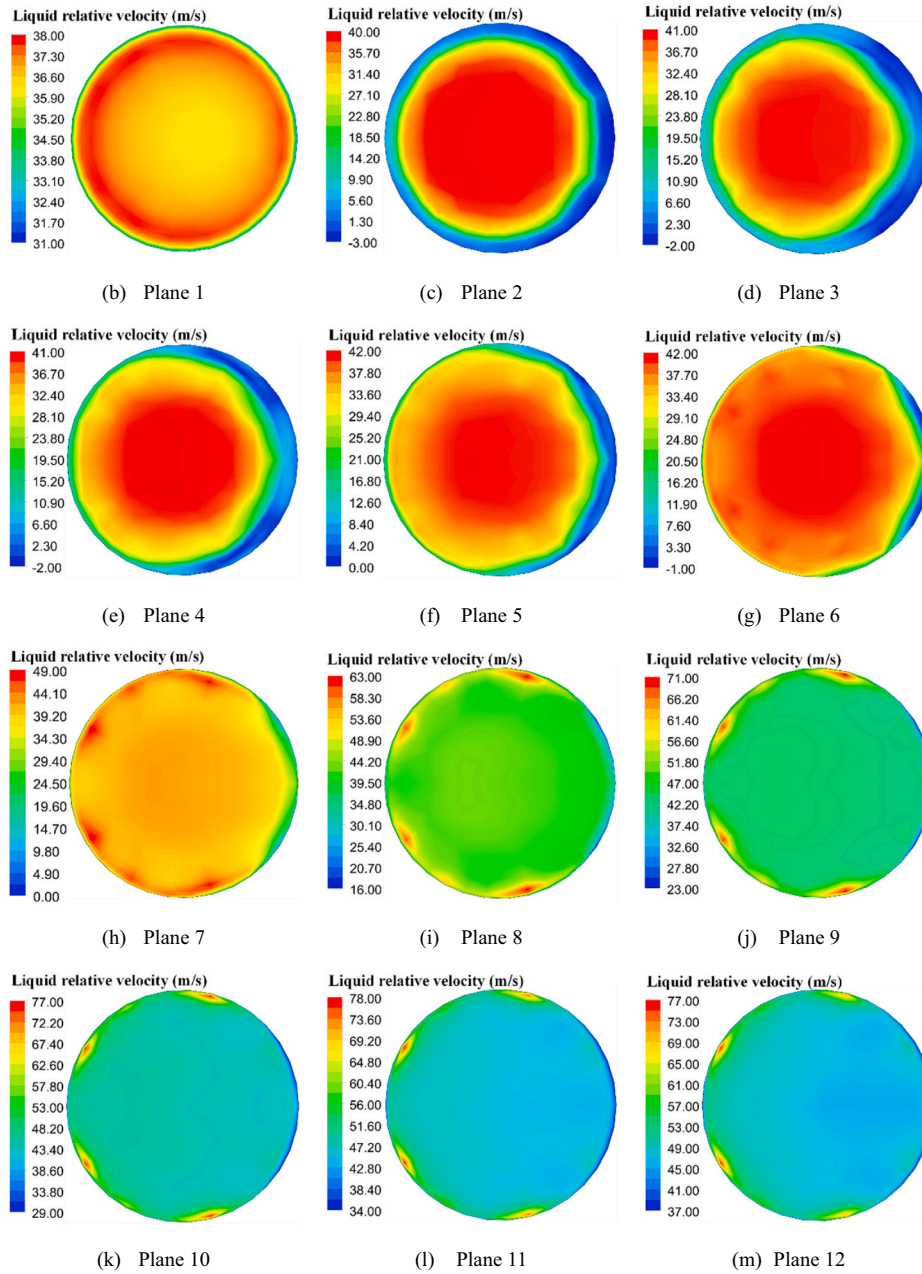
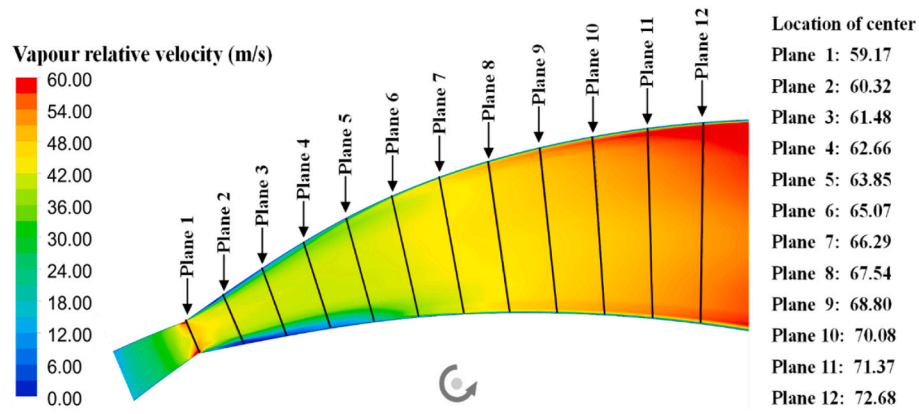


Fig. 8. Liquid relative velocity in cross-sections near the throat at 4623 rpm.



(a) The magnitude of vapour relative velocity on mid-plane

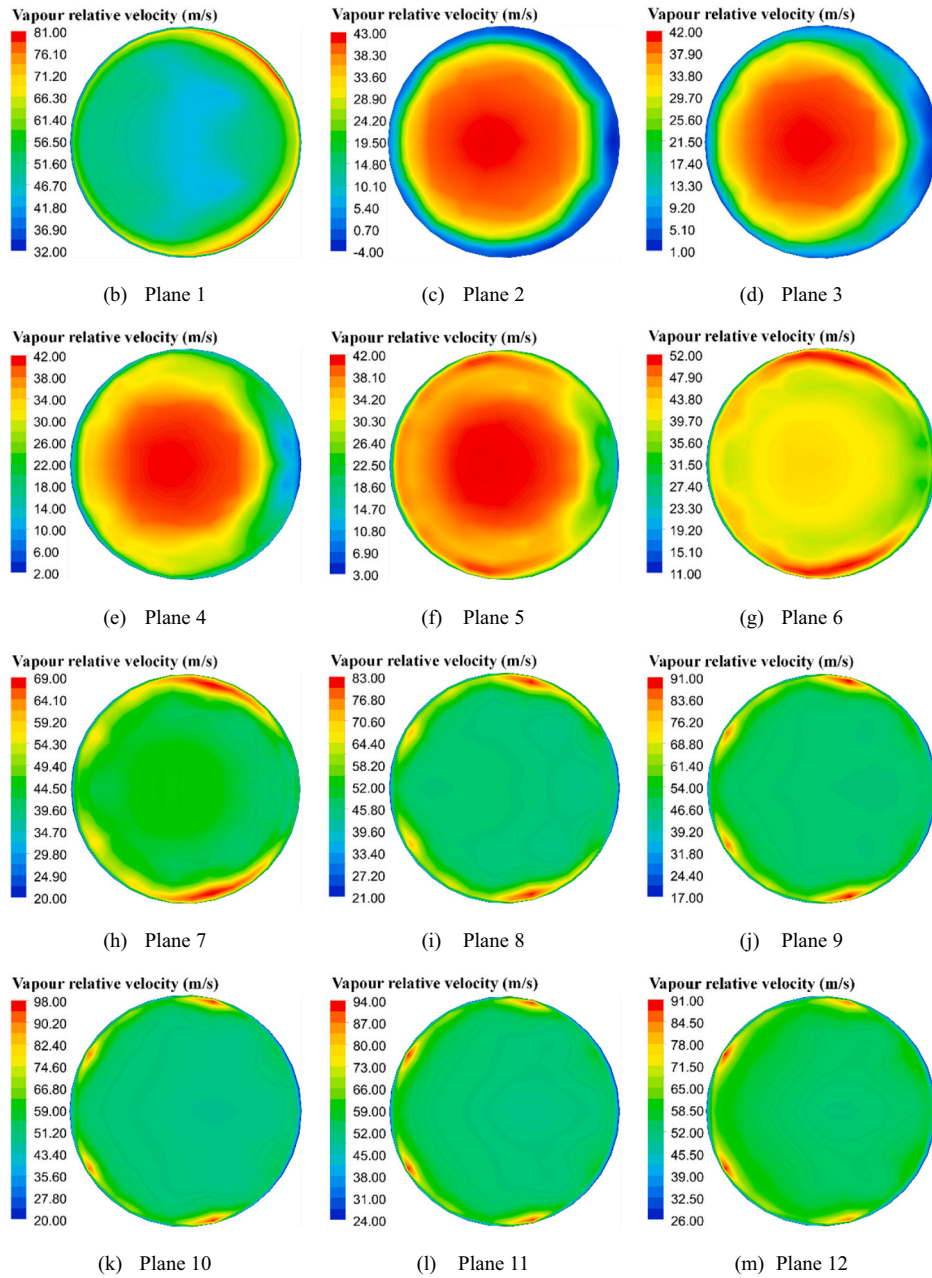


Fig. 9. Vapour relative velocity in cross-sections near the throat at 4623 rpm.

centerline. The pressure line represents the outer wall, and the suction line represents the inner wall. The R_{curv} is the local curvature radius of the centerline.

The conservation equations for the inviscid, flashing and rotating flow include continuity equation, momentum equation and energy equation in the noninertial system. The continuity equation for the total two-phase flow reads as

$$\frac{d}{dx} \left[\alpha \rho_v \bar{W}_v A^x + (1 - \alpha) \rho_l \bar{W}_l A^x \right] = 0 \quad (2)$$

Eq. (2) represents that the mass flow rate in the channel is constant, so it also can be rewritten as

$$\frac{d}{dx} \left\{ \left[\frac{\alpha(\rho_v \sigma - \rho_l)}{\rho_l} + 1 \right] \rho_l \bar{W}_l A^x \right\} = 0 \quad (3)$$

where $\sigma = W_v/W_l$. If the inviscid flow is assumed, the momentum equation along the flow direction is

$$\begin{aligned} \frac{d}{dx} \left\{ \left[\frac{\alpha(\rho_v \sigma^2 - \rho_l)}{\rho_l} + 1 \right] \rho_l \bar{W}_l^2 A^x \right\} = & -\frac{d}{dx} (A^x P) - \frac{d}{dx} (A^x P)_f \\ & + \left[\frac{\alpha(\rho_v - \rho_l)}{\rho_l} + 1 \right] \rho_l \Omega^2 R \cos \gamma A^x \end{aligned} \quad (4)$$

The second term on the right of Eq. (4) is frictional pressure reduction. Three coefficients can be defined as

$$\begin{cases} \Phi_1 = \alpha \left(\frac{\rho_v}{\rho_l} - 1 \right) + 1 \\ \Phi_2 = \alpha \left(\sigma \frac{\rho_v}{\rho_l} - 1 \right) + 1 \\ \Phi_3 = \alpha \left(\sigma^2 \frac{\rho_v}{\rho_l} - 1 \right) + 1 \end{cases} \quad (5)$$

As illustrated in Fig. 11, although the three coefficients should be different, they are almost equal to each other because the ratio of the density between liquid and vapour is low and close to zero. These coefficients are varied with the rotational speed insignificantly. At the section downstream the throat, there is a certain deviation, which reaches the largest at about 90 mm. Before the throat, all coefficients are equal to one, which indicates the flow in the channel can be treated as the single-phase flow. After the throat, the coefficients decreases remarkably with the length of the channel.

The dimensionless continuity equation can be derived as

$$\left[\frac{\pi \rho_{ref} W_{ref} R_{s,ref}^2}{x_{ref}} \right] \frac{d}{dx} \left(\Phi_2 \hat{\rho}_l \hat{W}_l \hat{A}^x \right) = 0 \quad (6)$$

with $\hat{W}_l^x = \bar{W}_l/W_{ref}$, $\hat{\rho}_l = \rho_l/\rho_{ref}$, $\hat{x} = x/x_{ref}$ and $\hat{A}^x = A^x/(\pi R_{s,ref}^2)$. Eq. (6) can be simplified as

$$\frac{d}{dx} \left(\Phi_2 \hat{\rho}_l \hat{W}_l \hat{A}^x \right) = 0 \quad (7)$$

The dimensionless momentum equation can be derived as

$$\begin{aligned} \left[\frac{W_{ref}}{\Omega_{ref} R_{ref}} \frac{R_{ref}}{x_{ref}} \right] \frac{d}{d\hat{x}} \left(\Phi_3 \hat{\rho}_l \hat{A}^x \hat{W}_l^2 \right) = & -\frac{d}{d\hat{x}} (\hat{A}^x \hat{P}) - \frac{d}{d\hat{x}} (\hat{A}^x \hat{P})_f \\ & + \left[\frac{\Omega_{ref} R_{ref}}{W_{ref}} \right] \Phi_1 \hat{\rho}_l \hat{\Omega}^2 \hat{R} \cos \gamma \hat{A}^x \end{aligned} \quad (8)$$

with $\hat{R} = R/R_{ref}$, $\hat{\Omega} = \Omega/\Omega_{ref}$ and $\hat{P} = P/(W_{ref} \rho_{ref} \Omega_{ref} x_{ref})$. Eq. (8) can be rewritten as

$$Ro T_R \frac{d}{d\hat{x}} \left(\Phi_3 \hat{\rho}_l \hat{A}^x \hat{W}_l^2 \right) = -\frac{d}{d\hat{x}} (\hat{A}^x \hat{P}) - \frac{d}{d\hat{x}} (\hat{A}^x \hat{P})_f + \frac{1}{Ro} \Phi_1 \hat{\rho}_l \hat{\Omega}^2 \hat{R} \cos \gamma \hat{A}^x \quad (9)$$

where Rossby number Ro is $W_{ref}/(\Omega_{ref} R_{ref})$ and T_R is R_{ref}/x_{ref} . The relative total pressure is defined as

$$P'_{rel} = P + \frac{\rho_l}{2} (\Phi_3 \bar{W}^2 + \Phi_1 U^2) \quad (10)$$

4.2. Average flow parameters

Eqs. (6) and (8) are useful for analyzing the rotating flashing flow because they show that there may be an analogy between the rotating single-phase flow and the rotating flashing flow. However, as shown in Fig. 5(a) and (b), the pressure and the liquid relative velocity of the rotating flashing flow are different from those of the rotating single-phase flow. The distinctive flow features of the rotating flashing flow are caused by the vaporization near the throat and the development of the vaporization downstream the throat.

The ratio of the pressure reduction ε_{dP} is proportional to the square of the ratio of the rotational speed ε_Ω before the throat and remains almost constant downstream the throat, as illustrated in Fig. 12. The ratio of the pressure reduction is defined as Eq. (11). The ratio of the rotational speed ε_Ω is the ratio between the operating rotational speed and 4623 rpm. Straight lines in Fig. 13 are derived by the square of the ratio of rotational speed.

$$\varepsilon_{dP} = \left(\frac{\Delta P}{\Delta L} \right)_\Omega / \left(\frac{\Delta P}{\Delta L} \right)_{4623 \text{ rpm}} \quad (11)$$

The maximum pressure in Fig. 5(a) is $P_{throat0}$ and the pressure at the throat is $P_{throat1}$, which is assumed to be equal to the corresponding local vaporization pressure. The static pressure at the entrance of the turbine P_{inlet} is constant under various rotational speeds. According to Eq. (11), the maximum pressure under a certain rotational speed ($P_{throat0}$)_N can be derived as

$$(P_{throat0})_\Omega = (1 - \varepsilon_{dP}) P_{inlet} + \varepsilon_{dP} (P_{throat0})_{4623 \text{ rpm}} \quad (12)$$

If the relative total pressure at the throat is assumed to be the same as the value at the maximum pressure, thus Eq. (13) can be derived

$$\begin{aligned} (P_{throat0})_\Omega + \frac{\rho_{l,throat0}}{2} \left(\Phi_{2,throat0} \varepsilon_W^2 \bar{W}_{throat0}^2 - \Phi_{1,throat0} \varepsilon_\Omega^2 U_{throat0}^2 \right) = \\ P_v + \frac{\rho_{l,throat1}}{2} \left(\Phi_{2,throat1} \varepsilon_W^2 \bar{W}_{throat1}^2 - \Phi_{1,throat1} \varepsilon_\Omega^2 U_{throat1}^2 \right) \end{aligned} \quad (13)$$

Substitute Eq. (12) into Eq. (13), the ratio of the relative velocity ε_W can be derived as illustrated in Eq. (14) and shown in Fig. 14.

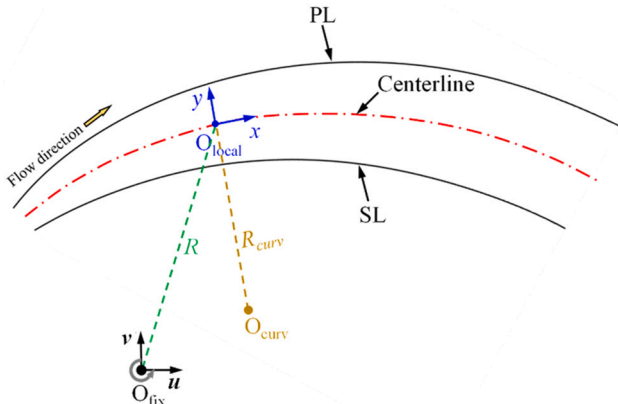


Fig. 10. The Frenet coordinate system in the curved rotating channel.

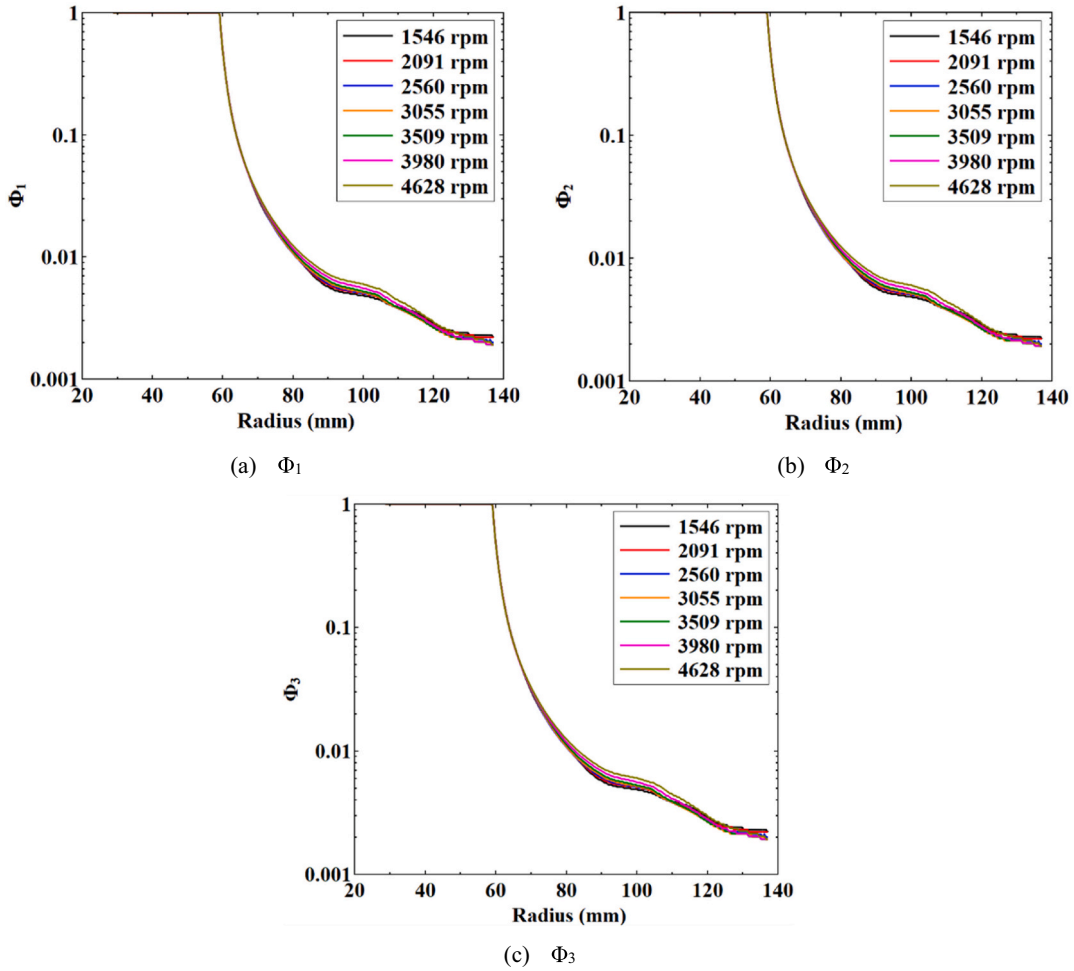


Fig. 11. Coefficients along the direction of the center line under various rotational speeds.

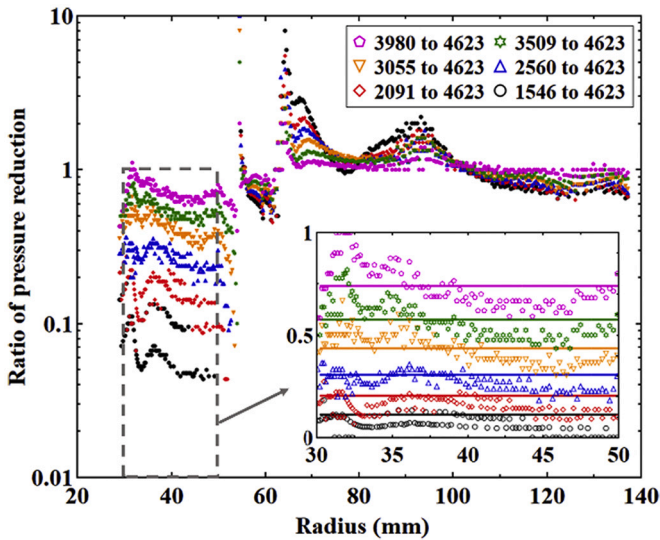


Fig. 12. The distribution of the ratio of pressure reduction along the center line under various rotational speeds and the ratio of the rotational speed.

$$\varepsilon_W = \sqrt{\varepsilon_\Omega^2 + \frac{1 - \varepsilon_\Omega^2}{\Phi_{2,throat0}} \frac{2(P_{inlet} - P_v)}{\rho_{l,throat0} (\bar{W}_{throat1}^2 - \bar{W}_{throat0}^2)}} \quad (14)$$

It should be noted that ε_W corresponds to the variation of the mass flow rate under various rotational speeds for the rotating flashing flow. It can be found in Fig. 13(a) that before the throat the predicted ratios of the relative velocity by using Eq. (14) agree with the averaged values obtained from the CFD, but after the throat, the predicted ratios start deviating from CFD results due to the phase change. If the relative liquid velocity \bar{W}_l is modified with $\Phi_2 \bar{W}_l$ according to Eq. (7), the predicted ratios agree with the CFD in the entire channel, as shown in Fig. 13(b).

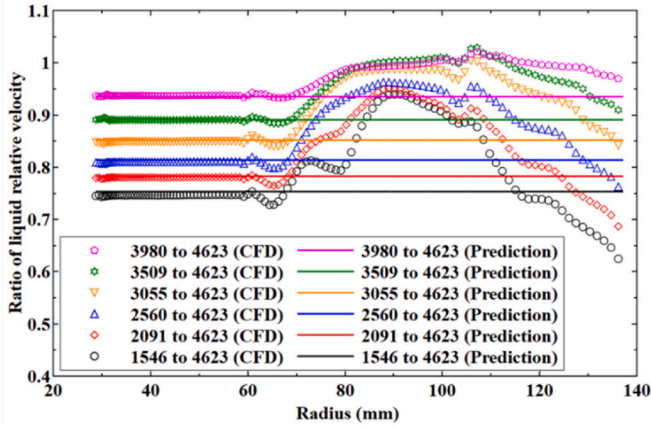
According to Eqs. (6) and (8), for the pure liquid flow, it can be derived that an imaginary area of the channel A^0 is $C_0/(\rho_l \bar{W}_l)$ when the local pressure is P . For the flashing flow, the area A_p is $C_0/(\Phi_2 \rho_l \bar{W}_l)$ at the same pressure. The dimensionless thickness of the vapour ring δ_r^* can be derived as

$$\delta_r^* = \frac{1}{\Phi_2} - 1 \quad (15)$$

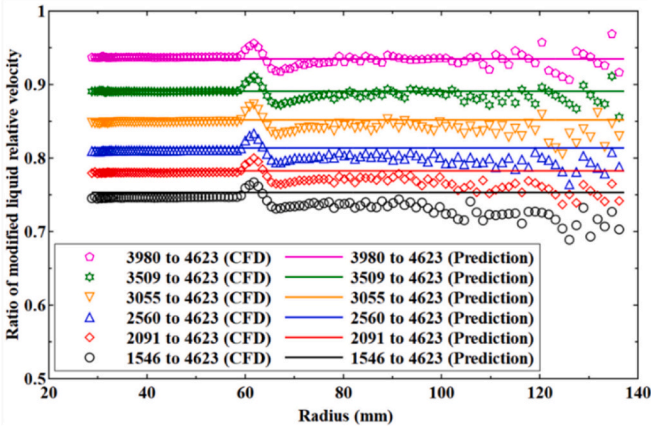
Eq. (15) can be also rewritten as

$$\alpha = \left[\frac{1}{(1 + \delta_r^*)^2} - 1 \right] \frac{1}{\sigma \rho_v / \rho_l - 1} \quad (16)$$

If a pure liquid core with a constant radius is assumed near the throat and the radius is equal to the radius of the throat, δ_r^* can be evaluated as



(a) The ratio of liquid relative velocity



(b) The ratio of modified liquid relative velocity

Fig. 13. Distribution of the ratio of liquid relative velocity and modified liquid relative velocity along the centerline under various rotational speeds.

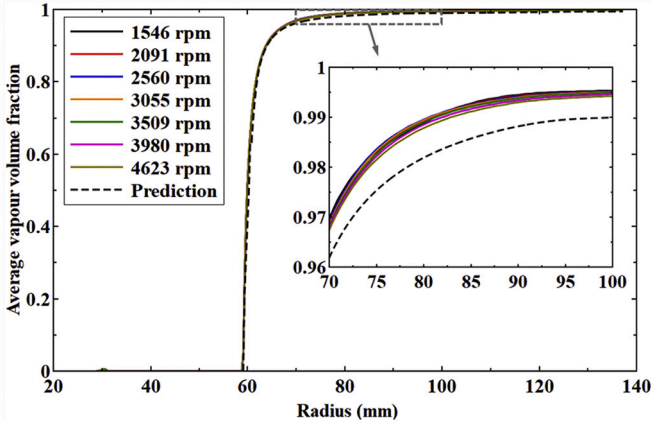


Fig. 14. Distribution of average vapour volume fraction along the centerline under various rotational speeds.

$$\delta_r^* = \frac{\sqrt{A^x} - \sqrt{A_{throat0}}}{\sqrt{A_{throat0}}} \quad (17)$$

Thus, if the variation of density is neglected and there is no slip between the two phases, the vapour volume fraction averaged on cross-sections along the direction of the center line with a given geometry of the channel can be predicted

$$\alpha' = \begin{cases} 0 & L \leq L_{throat} \\ \left[1 - \frac{1}{(1 + \delta_r^*)^2} \right] \frac{1}{1 - \rho_{v0}/\rho_{l0}} & L > L_{throat} \end{cases} \quad (18)$$

The predicted vapour volume fraction is illustrated in Fig. 14 and agrees with the three-dimensional results. Eq. (18) indicates that the distribution of the average vapour volume fraction is only dependent on the geometry of the channel in the divergence section and the density of the fluid. Because the ratio of density between the vapour water and the liquid water is nearly zero, the vapour volume fraction is mostly affected by the geometry, rather than the rotational speed. However, it should be noted that there is still a small deviation of the vapour volume fraction among different rotational speeds.

4.3. Flow profile analysis

In the rotating channel, there would be circulation on cross-sections since both the Coriolis force and the centrifugal force are exerted on the fluid. In the curved rotating channel, the additional centripetal force would be generated caused by the curvature of the channel. The secondary flow in the rotating flashing curved channel is different from that of the single-phase flow. As illustrated in Fig. 5, the primary fluid before the throat is liquid, while it changes to the vapour flow after a distance downstream the throat since the vapour volume fraction is close to one. Near the nozzle, the flow is complex because there is flashing inception and development, vapour ring, liquid core, and liquid attachment, etc. From the distribution of the average relative velocity, the velocity keeps almost constant after the throat and increases gradually because of the inertial effect of the liquid core. Thus, the flow profile can be distinctive in the entire channel, and the evolution of the secondary flow covers not only the Coriolis, the centrifugal and the centripetal effects, but also effects caused by interphase momentum exchange between the two phases including the slip and the interphase mass transfer.

The development of the secondary flow in the rotating flashing channel is different from that in the single-phase flow. To discuss the characteristic of the secondary flow, twelve cross-sections are cut normal to the center line as shown in Fig. 15. Plane 4 is the cross-section at the throat. The cross-sections are distributed uniformly along the direction of the center line to show the evolution of the secondary flow in the rotating flashing curved channel. However, it should be noted that the positions of these cross-sections are different from those in Figs. 6, 7 and 8, which only cover a short region near the throat.

Fig. 16 illustrates the vectors and streamlines of the modified liquid relative velocity in cross-sections at 4623 rpm. The vectors are normalized and projected on the tangential direction of the cross-section to show the flow profile in the normal direction. The left side is the pressure side, and the right side is the suction side. Before the throat, there is strong secondary flow caused by the inlet geometry of the channel near the pressure side, but it is weakened along the direction of the center line as shown in Fig. 16(a), (b) and (c). It can also be found that the direction of vortices in the upper half part of Fig. 16(a) and (b) is clockwise and opposite to that in the lower half part. In Fig. 16(c) and (d), the direction of vectors points to a center and the center moves in the direction from the suction side to the center of the cross-section. The concentration effect is caused by the convergent geometry of the channel. In Fig. 16(e), (f) and (g), the direction of vectors points to the edge of the cross-section and is opposite to that in Fig. 16(c) and (d). The divergence effect is caused by the divergent geometry of the channel. From Fig. 16(g) to (m), there are vortices developed near the suction side. But it should be noted that the direction of vortices is counter-clockwise in the upper half and adverse to that in Fig. 16(a) and (b).

Fig. 17 illustrates the flow profile at 1546 rpm. It can be found that the secondary flow is weaker in Fig. 17(a) than that in Fig. 16(a) and (b). From Fig. 17(g) to (m), vortices near the suction side are more obvious than those in Fig. 16(g) to (m). Thus, the rotation affects the secondary

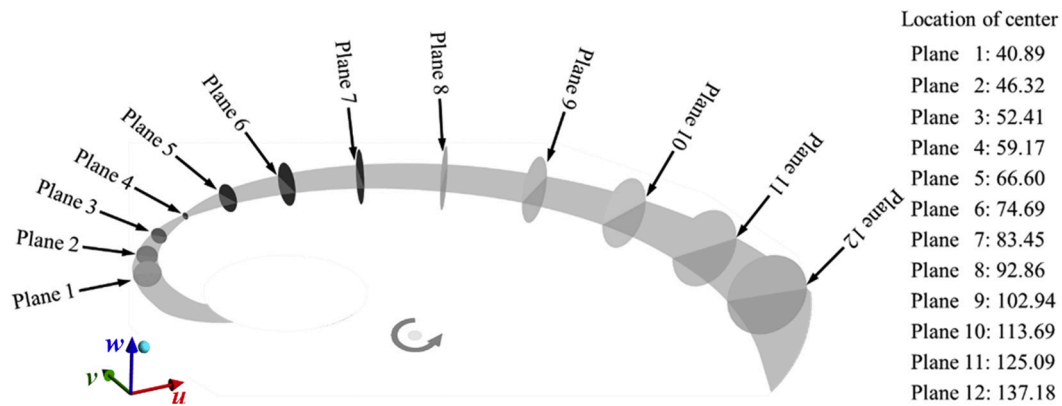


Fig. 15. Cross-planes for analyzing the secondary flow.

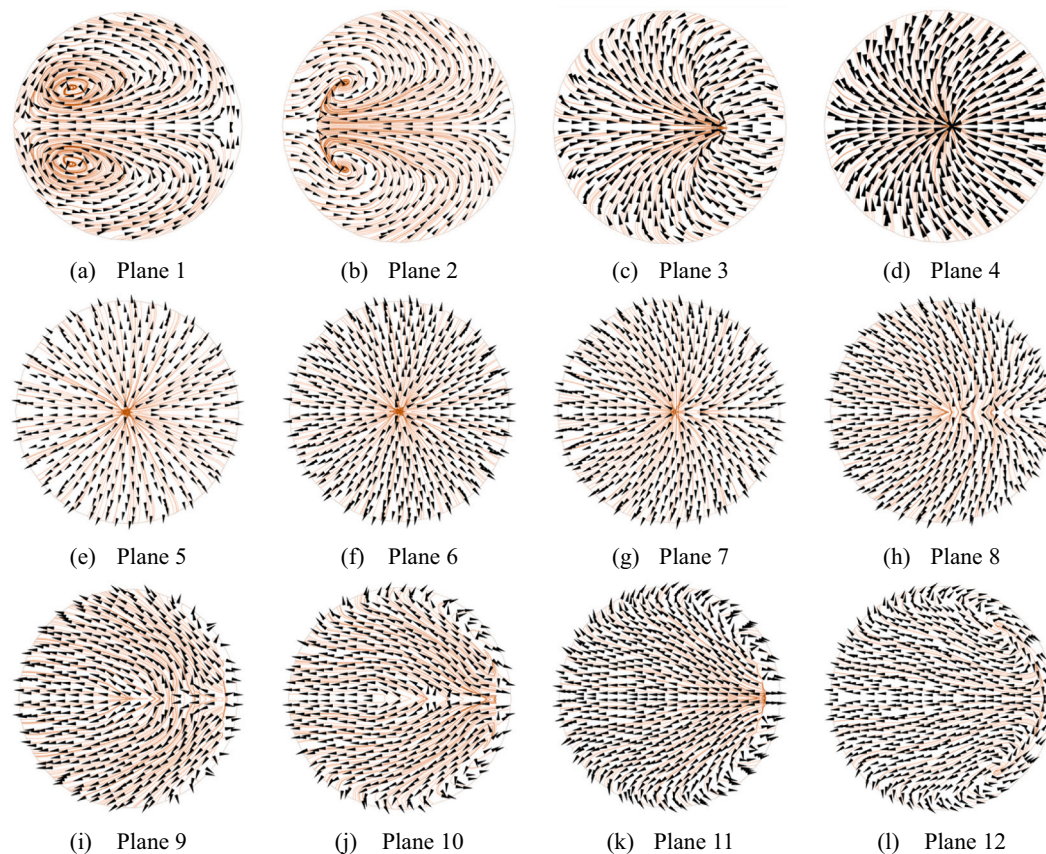


Fig. 16. The modified liquid relative velocity vectors and streamlines in cross-sections at 4623 rpm.

flow differently before the throat and after the throat. Before the throat, the secondary flow is more remarkable as the rotational speed is higher. However, after the throat, the secondary flow is weaker as the rotational speed increases. The flashing inception near the throat has the effect of homogenizing the flow in the normal direction of the cross-section.

5. Conclusion

In this paper, the internal flow in a curved rotating flashing channel with variable cross-section is analyzed according to numerical simulation results validated with experimental results. The average flow parameters, the vapour ring and the secondary flow are distinctive flow features of the flashing flow in the channel. The ratio of the pressure reduction is proportional to the square of the ratio of the rotational

speed before the throat. The ratio of the relative liquid velocity before the throat is equal to the ratio of the mass flow rate and formulated using the derived continuity and momentum equations in the Frenet coordinate system. The vapour ring is generated at the throat and accompanied by the liquid core in its inner side, and backflow and low-velocity zones can also be found in the vapour ring. Before the throat, the secondary flow is more significant as the rotational speed is higher. After a distance downstream the throat, the secondary flow gets weaker as the rotational speed increases. The rotational direction of the cell downstream the throat is opposite to that upstream the throat. The flashing inception near the throat has the effect on flow homogenizing in the normal direction of the cross-section.

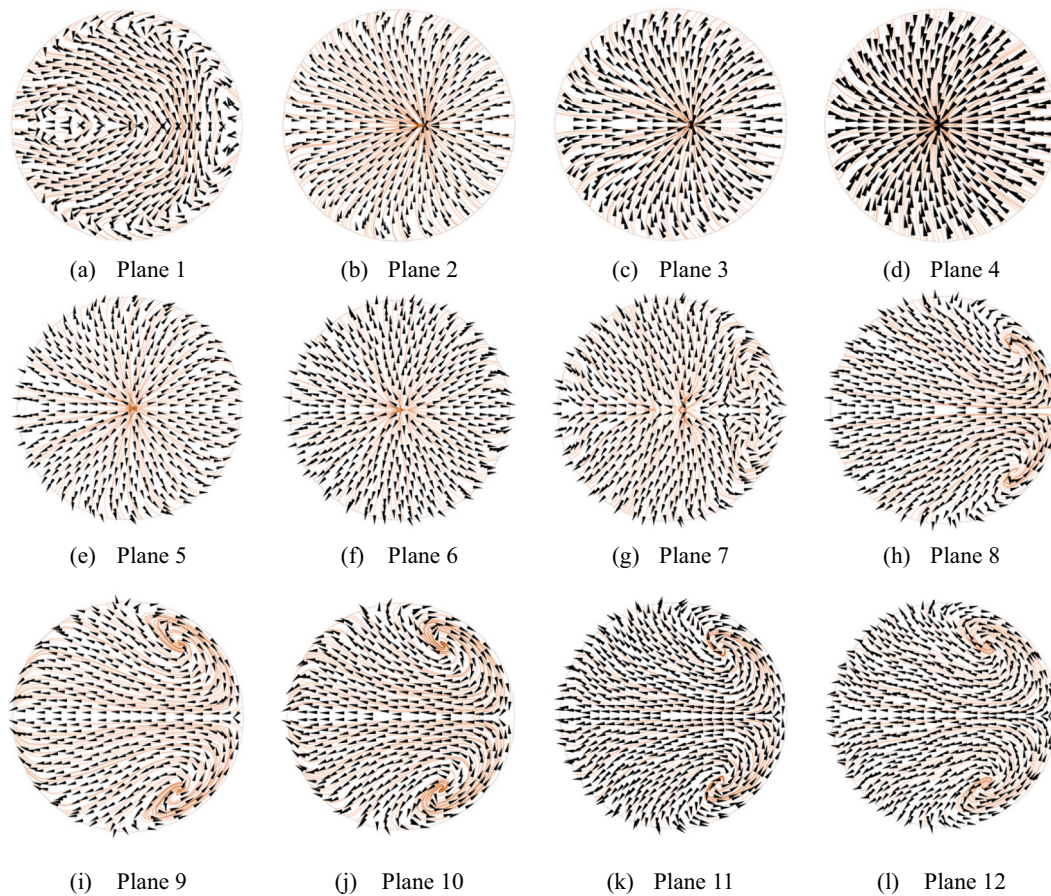


Fig. 17. The modified liquid relative velocity vectors and streamlines in cross-sections at 1546 rpm.

Nomenclature

Abbreviations

CFD	Computational fluid dynamics
LNG	Liquefied natural gas

Latin character

A	Area
C_D	Drag coefficient
D_b	Bubble diameter
D_d	Droplet diameter
Ja	Jakob number
La	Laplace number
m	Mass flow rate
\dot{m}_{lv}	Interphase mass transfer
Nu	Nusselt number
P	Pressure
Pe	Peclet number
R	Radius
R_s	Radius of cross-section
R_{curv}	Curvature radius
u, v, w	Coordinate axes in Cartesian coordinate system
W	Relative velocity
x, y	Coordinate axes in Frenet coordinate system
x_g	Vapour mass fraction

Greek Symbols

α	Vapour volume fraction
ε	Coefficient of the ratio
Φ_1, Φ_2, Φ_3	Two-phase coefficients
γ	Relative flow angle
κ	Curvature
ρ	Density
σ	Slip ratio
Ω	Angular speed

Superscripts

*	Ideal state
---	-------------

Subscripts

f	Friction
l	Liquid
ref	Reference
throat0	Before the throat
throat1	At the throat
v	Vapour

Author contributions

H.L. mainly contributes in methodology, investigation, CFD, flow analysis and original draft preparation; Z.Y. mainly contributes in conceptualization, review and editing, project administration and funding acquisition. Both authors have read and agreed to the published version of the manuscript.

Declaration of Competing Interest

We confirm that this work is original and has not been published elsewhere, nor is it currently under consideration for publication elsewhere.

We have no conflicts of interest to disclose.

Acknowledgement

The authors would like to acknowledge the Engineering and Physical Sciences Research Council (EP/P028829/1, EP/N020472/1, EP/R003122/1) in United Kingdom. Authors would also like to thank Dr. Abhijit Date, RMIT, Australia, for providing the reference turbine test data for development and validation of the CFD model. Authors would like to thank Dr. Sham Rane, City, University of London, United Kingdom, for providing numerical models for simulation of the internal flow in the two-phase reaction turbine. Authors would also like to thank Dr. Wenguang Li, University of Glasgow, United Kingdom, for reviewing this paper.

References

- [1] J.C. Jo, J.J. Jeong, B.J. Yun, J. Kim, Numerical analysis of subcooled water flashing flow from a pressurized water reactor steam generator through an abruptly broken main feed water pipe, *J. Press. Vessel Technol.* 141 (2019) 044501, <https://doi.org/10.1115/1.4043297>.
- [2] J. Lee, R. Madabhushi, C. Fotache, S. Gopalakrishnan, D. Schmidt, Flashing flow of superheated jet fuel, *Proc. Combust. Inst.* 32 (2009) 3215–3222, <https://doi.org/10.1016/j.proci.2008.06.153>.
- [3] S. Gopalakrishnan, D.P. Schmidt, A computational study of flashing flow in fuel injector nozzles, *SAE Int. J. Engines* 1 (2008) 160–170, <https://doi.org/10.4271/2008-01-0141>.
- [4] W. Angielczyk, Y. Bartosiewicz, D. Butrymowicz, Development of delayed equilibrium model for CO₂ convergent-divergent nozzle transonic flashing flow, *Int. J. Multiph. Flow* 131 (2020) 103351, <https://doi.org/10.1016/j.ijmultiphaseflow.2020.103351>.
- [5] T.H. Nigim, J.A. Eaton, CFD prediction of the flashing processes in a MSF desalination chamber, *Desalination* 420 (2017) 258–272, <https://doi.org/10.1016/j.desal.2017.06.026>.
- [6] L. Bolle, P. Downar-Zapolski, J. Franco, J.M. Seynhaeve, Experimental and theoretical analysis of flashing water flow through a safety valve, *J. Hazard. Mater.* 46 (1996) 105–116, [https://doi.org/10.1016/0304-3894\(95\)00062-3](https://doi.org/10.1016/0304-3894(95)00062-3).
- [7] R. Darby, On two-phase frozen and flashing flows in safety relief valves: recommended calculation method and the proper use of the discharge coefficient, *J. Loss Prev. Process Ind.* 17 (2004) 255–259, <https://doi.org/10.1016/j.jlp.2004.04.001>.
- [8] C. Ji, N. Wang, Z. Liu, Three-dimensional simulation of flash evaporation of non-uniform spray in saturated vapor environment, *Heat Mass Transf.* 56 (2020) 3289–3301, <https://doi.org/10.1007/s00231-020-02936-4>.
- [9] J. Chen, X. Gao, S. Bao, L. Hu, J. Xie, Numerical analysis of spray characteristics with liquid nitrogen, *Cryogenics (Guildf)* 109 (2020) 103113, <https://doi.org/10.1016/j.cryogenics.2020.103113>.
- [10] Y. Liao, D. Lucas, Possibilities and limitations of CFD simulation for flashing flow scenarios in nuclear applications, *Energies* 10 (2017) 139, <https://doi.org/10.3390/en10010139>.
- [11] Y. Liao, D. Lucas, 3D CFD simulation of flashing flows in a converging-diverging nozzle, *Nucl. Eng. Des.* 292 (2015) 149–163, <https://doi.org/10.1016/j.nucengdes.2015.06.015>.
- [12] H.E. Kimmel, S. Cathery, Thermo-fluid dynamics and design of liquid-vapour two-phase LNG expanders, in: *Gas Process. Assoc. Tech. Meet. Adv. Process Equipment*, Paris, Fr., Paris, France, 2010.
- [13] H. Li, W. Li, X. Zhang, Y. Zhu, Z. Zuo, H. Chen, Design method of a two-phase annular nozzle in cryogenic liquid expander, *Proc. Inst. Mech. Eng. Part A J. Power Energy* 233 (2019) 762–772, <https://doi.org/10.1177/0957650918822943>.
- [14] S. Rane, L. He, H. Ma, CFD modelling and analysis of two-phase geothermal energy turbine in project Combi-Gen, *Int Conf Innov. Appl. Energy*, Oxford (2019) 257, <https://doi.org/10.1093/jcde/qwaa020>.
- [15] H. Li, S. Rane, Z. Yu, G. Yu, An inverse mean-line design method for optimizing radial outflow two-phase turbines in geothermal systems, *Renew. Energy* 168 (2021) 463–490, <https://doi.org/10.1016/j.renene.2020.12.079>.
- [16] J.R. Riznic, M. Ishii, Bubble number density and vapor generation in flashing flow, *Int. J. Heat Mass Transf.* 32 (1989) 1821–1833, [https://doi.org/10.1016/0017-9310\(89\)90154-3](https://doi.org/10.1016/0017-9310(89)90154-3).
- [17] E. Elias, P.L. Chambré, Bubble transport in flashing flow, *Int. J. Multiph. Flow* 26 (2000) 191–206, [https://doi.org/10.1016/S0301-9322\(99\)00011-7](https://doi.org/10.1016/S0301-9322(99)00011-7).
- [18] T.S. Shin, O.C. Jones, Nucleation and flashing in nozzles—1. A distributed nucleation model, *Int. J. Multiph. Flow* 19 (1993) 943–964, [https://doi.org/10.1016/0301-9322\(93\)90071-2](https://doi.org/10.1016/0301-9322(93)90071-2).
- [19] V.N. Blinkov, O.C. Jones, B.I. Nigmatulin, Nucleation and flashing in nozzles—2. Comparison with experiments using a five-equation model for vapor void development, *Int. J. Multiph. Flow* 19 (1993) 965–986, [https://doi.org/10.1016/0301-9322\(93\)90072-3](https://doi.org/10.1016/0301-9322(93)90072-3).
- [20] J.C. Leung, A generalized correlation for one-component homogeneous equilibrium flashing choked flow, *AIChE J.* 32 (1986) 1743–1746, <https://doi.org/10.1002/aic.690321019>.
- [21] W. Angielczyk, J.M. Seynhaeve, J. Gagan, Y. Bartosiewicz, D. Butrymowicz, Prediction of critical mass rate of flashing carbon dioxide flow in convergent-divergent nozzle, *Chem. Eng. Process. - Process Intensif.* 143 (2019) 107599, <https://doi.org/10.1016/j.cep.2019.107599>.
- [22] J.C. Leung, M.A. Grolmes, A generalized correlation for flashing choked flow of initially subcooled liquid, *AIChE J.* 34 (1988) 688–691, <https://doi.org/10.1002/aic.690340421>.
- [23] O.C. Jones Jr., Flashing inception in flowing liquids, *J. Heat Transf.* 102 (1980) 439–444, <https://doi.org/10.1115/1.3244319>.
- [24] M. Alamgir, J.H. Lienhard, Correlation of pressure undershoot during hot-water depressurization, *J. Heat Transf.* 103 (1981) 52–55, <https://doi.org/10.1115/1.3244429>.
- [25] A. Attou, J.M. Seynhaeve, Steady-state critical two-phase flashing flow with possible multiple choking phenomenon: part 2: comparison with experimental results and physical interpretations, *J. Loss Prev. Process Ind.* 12 (1999) 347–359, [https://doi.org/10.1016/S0950-4230\(98\)00018-7](https://doi.org/10.1016/S0950-4230(98)00018-7).
- [26] B.J.C. Wu, N. Abuaf, P. Saha, Study of nonequilibrium flashing of water in a converging-diverging nozzle, in: *Modeling vol 2*, Brookhaven National Lab., Upton, New York, United States, 1981.
- [27] A. Manera, H.-M. Prasser, D. Lucas, T.H.J.J. van der Hagen, Three-dimensional flow pattern visualization and bubble size distributions in stationary and transient upward flashing flow, *Int. J. Multiph. Flow* 32 (2006) 996–1016, <https://doi.org/10.1016/j.ijmultiphaseflow.2006.03.005>.
- [28] X.-S. Wang, B. Chen, R. Wang, H. Xin, Z.-F. Zhou, Experimental study on the relation between internal flow and flashing spray characteristics of R134a using straight tube nozzles, *Int. J. Heat Mass Transf.* 115 (2017) 524–536, <https://doi.org/10.1016/j.ijheatmasstransfer.2017.08.040>.
- [29] J.W. Gärtner, A. Kronenburg, A. Rees, J. Sender, M. Oschwald, G. Lamanna, Numerical and experimental analysis of flashing cryogenic nitrogen, *Int. J. Multiph. Flow* 130 (2020) 103360, <https://doi.org/10.1016/j.ijmultiphaseflow.2020.103360>.
- [30] M. Moulaï, R. Grover, S. Parrish, D. Schmidt, Internal and near-nozzle flow in a multi-hole gasoline injector under flashing and non-flashing conditions, in: *SAE Technical Paper* 2015-01-0944, 2015, <https://doi.org/10.4271/2015-01-0944>.
- [31] J.P. Janet, Y. Liao, D. Lucas, Heterogeneous nucleation in CFD simulation of flashing flows in converging-diverging nozzles, *Int. J. Multiph. Flow* 74 (2015) 106–117, <https://doi.org/10.1016/j.ijmultiphaseflow.2015.04.005>.
- [32] Y. Liao, D. Lucas, 3D CFD simulation of flashing flows in a converging-diverging nozzle, *Nucl. Eng. Des.* 292 (2015) 149–163, <https://doi.org/10.1016/j.nucengdes.2015.06.015>.
- [33] B. Ebrahimi, G. He, Y. Tang, M. Franchek, D. Liu, J. Pickett, F. Springett, D. Franklin, Characterization of high-pressure cavitating flow through a thick orifice plate in a pipe of constant cross section, *Int. J. Therm. Sci.* 114 (2017) 229–240, <https://doi.org/10.1016/j.ijthermalsci.2017.01.001>.
- [34] J. Zhu, S. Elbel, Experimental investigation of a novel expansion device control mechanism: vortex control of initially subcooled flashing R134a flow expanded through convergent-divergent nozzles, *Int. J. Refrig.* 85 (2018) 167–183, <https://doi.org/10.1016/j.jrefrig.2017.09.023>.
- [35] Q. Dang Le, R. Mereu, G. Besagni, V. Dossena, F. Inzoli, Computational fluid dynamics modeling of flashing flow in convergent-divergent nozzle, *J. Fluids Eng.* 140 (2018) 101102, <https://doi.org/10.1115/1.4039908>.
- [36] L. Geng, H. Liu, X. Wei, CFD analysis of the flashing flow characteristics of subcritical refrigerant R134a through converging-diverging nozzles, *Int. J. Therm. Sci.* 137 (2019) 438–445, <https://doi.org/10.1016/j.ijthermalsci.2018.12.011>.
- [37] J. Zhu, S. Elbel, CFD simulation of vortex flashing R134a flow expanded through convergent-divergent nozzles, *Int. J. Refrig.* 112 (2020) 56–68, <https://doi.org/10.1016/j.jrefrig.2019.12.005>.
- [38] S. Rane, L. He, CFD analysis of flashing flow in two-phase geothermal turbine design, *J. Comput. Des. Eng.* 7 (2020) 238–250, <https://doi.org/10.1093/jcde/qwaa020>.
- [39] A. Date, S. Vahaji, J. Andrews, A. Akbarzadeh, Experimental performance of a rotating two-phase reaction turbine, *Appl. Therm. Eng.* 76 (2015) 475–483, <https://doi.org/10.1016/j.applthermaleng.2014.11.039>.
- [40] A. Khaghani, Dual Thermal System for Power and Fresh Water Production, RMIT University, 2013. https://researchrepository.rmit.edu.au/esploro/outputs/doctoral/Dual-thermal-system-for-power-and-fresh-water-production/9921861234401341/files_and_links.

- [41] S. Rane, L. He, Two-phase flow analysis and design of geothermal energy turbine, in: IOP Conf. Ser. Mater. Sci. Eng., IOP Publishing, 2019, p. 12043, <https://doi.org/10.1088/1757-899X/604/1/012043>.
- [42] S. Rane, L. He, Modelling of flash boiling in two phase geothermal turbine, in: Proc. 16th UK Heat Transf. Conf., Nottingham, United Kindom, 2019, p. 005.
- [43] Y. Liao, D. Lucas, A review on numerical modelling of flashing flow with application to nuclear safety analysis, Appl. Therm. Eng. 182 (2021) 116002, <https://doi.org/10.1016/j.applthermaleng.2020.116002>.